

# 1 **Top-down modulation of stimulus drive via** 2 **beta-gamma cross-frequency interaction.**

3 Craig G. Richter<sup>1,5,\*</sup>, William H. Thompson<sup>1,2,5</sup>, Conrado A. Bosman<sup>3,4</sup> Pascal Fries<sup>1,3,\*</sup>

4 <sup>1</sup> Ernst Strüngmann Institute (ESI) for Neuroscience in Cooperation with Max Planck Society,  
5 Deutschordenstraße 46, 60528 Frankfurt, Germany

6 <sup>2</sup> Department of Clinical Neuroscience, Karolinska Institute, Nobels Väg 9, 171 77 Solna, Sweden

7 <sup>3</sup> Donders Institute for Brain, Cognition and Behaviour, Kapittelweg 29, Radboud University, 6525 EN  
8 Nijmegen, Netherlands

9 <sup>4</sup> Swammerdam Institute for Life Sciences, Center for Neuroscience, Faculty of Science, University of  
10 Amsterdam, Sciencepark 904, 1098 XH Amsterdam, Netherlands

11 <sup>5</sup> Co-first authors

12 \*Correspondence: [craig.richter@esi-frankfurt.de](mailto:craig.richter@esi-frankfurt.de), [pascal.fries@esi-frankfurt.de](mailto:pascal.fries@esi-frankfurt.de)

13

## 14 ABSTRACT

15 Recently, several studies have demonstrated that visual stimulus routing is subserved by inter-areal  
16 gamma-band synchronization, whereas top-down influences are mediated by alpha-beta band  
17 synchronization. These processes may implement top-down control if top-down and bottom-up  
18 mediating rhythms are coupled via cross-frequency interaction. To test this possibility, we investigated  
19 Granger-causal influences among awake macaque primary visual area V1, higher visual area V4 and  
20 parietal control area 7a during attentional task performance. Top-down 7a-to-V1 beta-band influences  
21 enhanced visually driven V1-to-V4 gamma-band influences. This enhancement was spatially specific  
22 and largest for a beta-to-gamma delay of ~100 ms, suggesting a causal relationship. We propose that  
23 this cross-frequency interaction mechanistically subserves the attentional control of stimulus selection.

24 Many cognitive effects in vision can only be explained by invoking the concept of top-down influences  
25 (Gilbert & Sigman, 2007). For example, when top-down influences can pre-allocate attention to  
26 specific spatial locations, stimulus processing is more accurate and/or faster, even when stimuli  
27 remain unaltered. Correspondingly, neurons in early and mid-level visual cortex show enhanced firing  
28 rates when processing attended stimuli. These neurophysiological consequences of top-down control  
29 need to be mediated by corresponding projections. Indeed, anatomical studies have documented  
30 projections in the top-down direction that are at least as numerous as bottom-up projections. Bottom-  
31 up and top-down projections show different characteristic laminar patterns of origin and termination,  
32 and the pattern of pairwise projections abides by a global hierarchy, in which each area occupies a  
33 particular hierarchical level (Felleman & Van Essen, 1991; Hilgetag, O'Neill, & Young, 1996; Markov et  
34 al., 2014). Recently, it has been shown that the pattern of anatomical projections is closely correlated  
35 to a pattern of frequency-specific directed inter-areal influences. Influences mediated by bottom-up  
36 projections are primarily carried by gamma-band synchronization in both macaque and human visual  
37 cortex; by contrast, influences mediated by top-down projections are primarily carried by alpha-beta-  
38 band synchronization (Bastos, Vezoli, et al., 2015b; Michalareas et al., 2016; van Kerkoerle et al.,  
39 2014). A similar association of higher frequency bands with bottom-up and lower frequency bands with  
40 top-down projections has been found also in the auditory system (Fontolan, Morillon, Liegeois-  
41 Chauvel, & Giraud, 2014) and the hippocampus (Bieri, Bobbitt, & Colgin, 2014; Colgin et al., 2009).

42 These relations between anatomy and physiology suggest that gamma rhythms are more involved in  
43 the bottom-up routing of stimulus information, whereas alpha-beta rhythms play a key role in  
44 modulating this process through top-down control (Bastos et al., 2012). In support of this, inter-areal  
45 gamma-band coherence is enhanced during tasks that involve primarily bottom-up stimulus routing  
46 (like pop-out), whereas inter-areal alpha-beta band coherence is enhanced during tasks that require  
47 top-down control (like visual search) (Buschman & Miller, 2007; Stein, vonStein, Chiang, König, &  
48 König, 2000). During sustained visual attention tasks, and probably also during much of natural  
49 viewing, top-down and bottom-up influences are both present simultaneously, with attentional top-  
50 down control persistently influencing bottom-up stimulus processing. The coexistence of both rhythms  
51 suggests the following scenario for attentional influences on visual processing: 1) Visual stimulation  
52 induces bottom-up gamma-band influences among visual areas; 2) Top-down beta-band influences  
53 are endogenously generated and thereby stimulus independent; 3) Attention enhances both, top-down  
54 beta-band and bottom-up gamma-band influences; 4) Cross-frequency interactions result in top-down  
55 beta-band influences enhancing subsequent bottom-up gamma-band influences in a spatially specific  
56 manner. There is substantial evidence for points 1) to 3), and this paper provides evidence for point 4).  
57 Regarding point 1): Gamma-band activity is induced by visual stimulation in lower visual areas (Gray,  
58 König, Engel, & Singer, 1989) and it entrains gamma in higher visual areas in a bottom-up manner  
59 (Bastos, Vezoli, et al., 2015b; Bosman et al., 2012; Grothe, Neitzel, Mandon, & Kreiter, 2012; Jia,  
60 Tanabe, & Kohn, 2013). Note that in higher visual areas, attention alone can induce gamma among  
61 local interneurons, and the projecting pyramidal cells join when visual stimulation commences (Vinck,  
62 Womelsdorf, Buffalo, Desimone, & Fries, 2013). Regarding point 2): Beta-band influences among  
63 visual areas are present before stimulus onset, and are typically stronger in the top-down direction  
64 (Bastos, Vezoli, et al., 2015b). Regarding point 3): Inter-areal gamma-band coherence and bottom-up  
65 gamma-band influences are enhanced by attention (Bosman et al., 2012; Grothe et al., 2012), and so  
66 are top-down beta-band influences (Bastos, Vezoli, et al., 2015b). In the present study, we will confirm  
67 points 1) – 3) for ECoG data recorded from two macaque monkeys, when they direct attention to the  
68 contralateral versus ipsilateral hemifield. To investigate point 4), we then analyze spontaneous  
69 fluctuations in top-down beta-band and bottom-up gamma-band influences and their mutual interplay.  
70 We find that on a moment-by-moment basis, top-down beta-band influences correlate positively with  
71 bottom-up gamma-band influences. Spontaneous enhancements in top-down beta-band influences  
72 were followed ~100 ms later by enhancements in bottom-up gamma-band influences, suggestive of a  
73 causal relation. Consistent with a role in selective attention, this effect was spatially specific, i.e.

74 bottom-up gamma-band influences depended most strongly on the top-down beta-band influences,  
75 that were directed to the origin of the bottom-up influence.

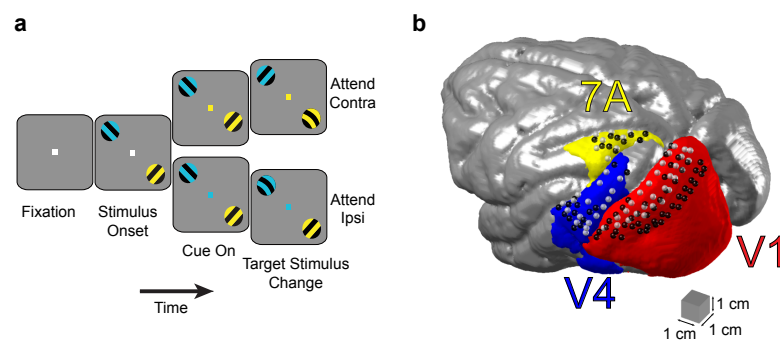
## 76 RESULTS

### 77 Top-down versus Bottom-up Spectral Asymmetries and their Stimulus and Task 78 Dependence

79 To assess the individual frequency bands for each monkey, we first computed the power spectral  
80 densities (PSD) during stimulation in two awake monkeys (monkey K and monkey P) for each region-  
81 of-interest (ROI) of two selected region-of-interest (ROI) pairs: 7A-V1 and V1-V4 (**Fig. 1a, b**). The ROI  
82 pair 7A-V1 was selected, because it constitutes a clear top-down pathway with documented  
83 projections from a very high-level control area to primary visual cortex (Bastos, Vezoli, et al., 2015b;  
84 Markov et al., 2014; Michalareas et al., 2016). The ROI pair V1-V4 was selected, because it  
85 constitutes a clear bottom-up pathway emerging from V1, i.e. the area targeted by the top-down  
86 7A→V1 influence. For both ROI pairs, the ECoG provided good coverage. Area 7A shows strong beta-  
87 band peaks in both monkeys (monkey K:  $\approx 17$  Hz; monkey P:  $\approx 13$  Hz) (**Fig. 2e, f**). Areas V1 and V4  
88 show gamma frequency peaks (monkey K:  $\approx 76$  Hz; monkey P:  $\approx 60$  Hz) (**Fig. 2a-d**). Beta activity is  
89 visible in V4 and V1 of both monkeys at their matching peak frequencies found in area 7A. In area V4  
90 of both monkeys, there are distinct beta peaks. In area V1, monkey K shows a distinct beta peak, and  
91 monkey P shows a shoulder in the power spectrum, at the respective beta frequency. We determined  
92 the dominant inter-areal communication frequencies for each monkey by calculating the pair-wise  
93 phase consistency (PPC), a frequency-resolved measure of synchronization (Vinck, van Wingerden,  
94 Womelsdorf, Fries, & Pennartz, 2010), between the V1-V4 and 7A-V1 ROI pairs (**Fig. 2g-j**). Gamma  
95 band synchronization was present for both ROI pairs in both monkeys with peaks at  $\approx 76$  Hz in monkey  
96 K and in a range of 58–65 Hz in monkey P. Beta peaks were present between both ROI pairs: at  $\approx 17$   
97 Hz in monkey K and at  $\approx 12$  Hz in monkey P. Some of the power and PPC spectra showed also a  
98 theta-band peak, which is not further investigated, because the focus of this study is on the interaction  
99 between beta and gamma rhythms. For the further analyses, data from both monkeys were combined,  
100 by aligning their individual beta and gamma peaks  $\pm 10$  Hz and averaging across monkeys.

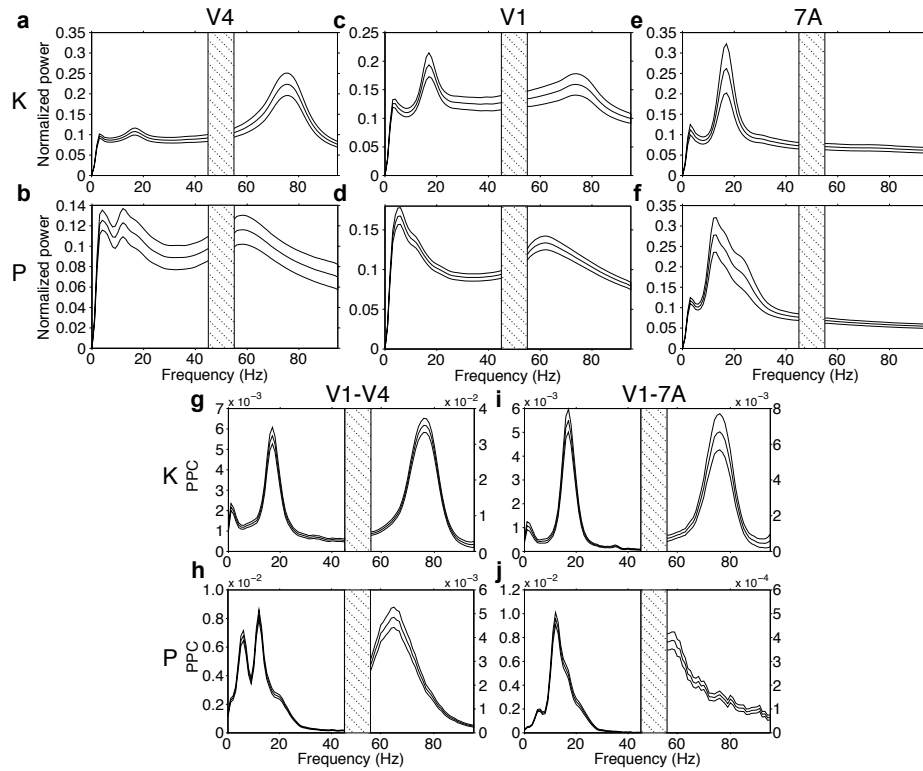
101 To demonstrate that inter-areal gamma-band synchronization is stimulus driven (Bosman et al., 2012;  
102 Grothe et al., 2012), we contrasted PPC between the fixation and stimulation conditions. **Fig. 3a, b**  
103 shows significantly enhanced gamma-band synchronization between ROI pairs V1-V4 and 7A-V1  
104 once the stimulus has appeared, in contrast to an almost flat spectrum when no stimulus is present.  
105 This finding is consistent with gamma-band oscillations occurring as a result of stimulus drive. In  
106 contrast, beta-band synchronization for both ROI pairs is present already during the pre-stimulus  
107 fixation period, suggesting an endogenous origin (**Fig. 3a, b**). Beta synchronization is maintained  
108 during the stimulation period, consistent with an ongoing top-down influence.

109 We next assessed the dominant directionality of interareal synchronization and its attentional  
110 modulation. We quantified directionality of synchronization by means of Granger causality (GC)  
111 (Bressler & Seth, 2011; Ding, Chen, & Bressler, 2006; Granger, 1969). As shown by Bastos et al.  
112 (2015b), and extended to humans by Michalareas et al. (2016), the top-down beta-band influence of  
113 area 7A to V1 is significantly greater than the bottom-up beta-band influence of V1 to 7A (**Fig. 3e**).  
114 This top-down beta-band influence is significantly increased when attention is directed to the visual  
115 hemifield contralateral to the recording grid (**Fig. 3c**), consistent with an earlier report (Bastos, Litvak,  
116 et al., 2015a). Between V1 and V4, the gamma-band influence is stronger in the bottom-up direction  
117 from area V1 to V4 (**Fig. 3f**). The bottom-up gamma-band influence of V1 to V4 was significantly  
118 increased with attention (**Fig. 3d**).



119  
120  
121  
122  
123  
124  
125

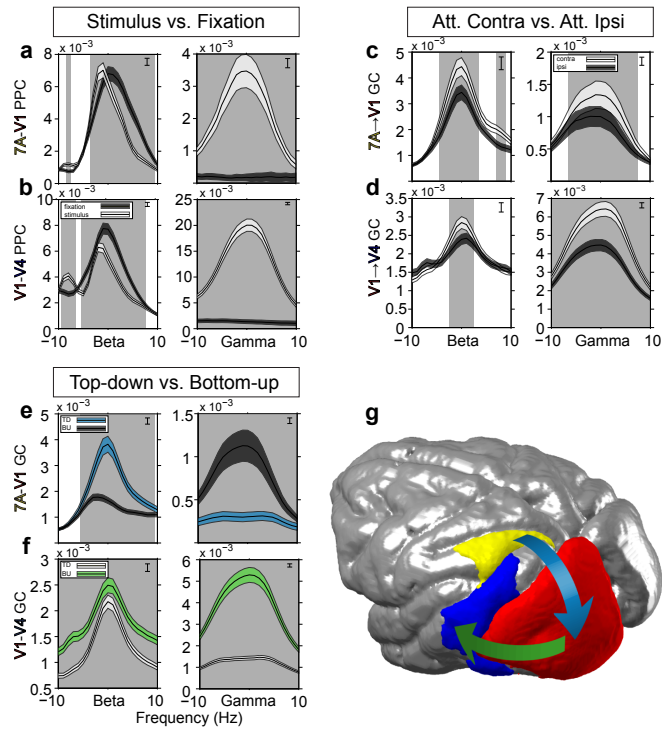
**Figure 1** Behavioral task and recording locations. (a) The task commenced with a fixation period followed by presentation of two differently colored stimuli. The fixation point color then indicated the visual stimulus to covertly attend in either the visual hemifield ipsilateral (ipsi) or contralateral (contra) to the recording grid. (b) Recording sites for areas V1/V2 (red), V4 (blue), and 7A (yellow) from monkey K (white spheres) and monkey P (black spheres), co-registered to a common macaque template.



126

127 **Figure 2** PSDs and PPC during stimulation. (a, b) V4, (c, d) V1, and 7A (e, f) power spectra averaged over all  
128 respective site pairs of monkey K (a, c, e) and P (b, d, f). (g - j) LFP-LFP PPC for V1-V4 (g, h) and V1-7A (i, j) for  
129 monkey K and P, respectively. Error bars show  $\pm 1$  standard error of the mean (SEM) over sites. Frequencies from  
130 45 – 55 Hz were omitted due to line-noise pollution.

131



132

133 **Figure 3** Average PPC and GC spectra. (a, b) LFP-LFP PPC for 7A-V1 (a) and V1-V4 (b) during fixation (dark  
 134 shading) and stimulation (light shading), averaged over all respective site pairs then averaged over monkeys after  
 135 alignment to their beta and gamma peak frequencies. Gray bars indicate frequency regions with significant  
 136 condition differences ( $p < 0.05$ , two-tailed non-parametric randomization test, corrected for comparisons across  
 137 multiple frequencies). Inset brackets denote the minimum separation required for significance. Error bars show  $\pm 1$   
 138 standard error of the mean (SEM) over site pairs. Frequencies from 45 – 55 Hz were omitted due to line-noise  
 139 pollution. (c, d) GC influence for 7A  $\rightarrow$  V1 (c) and V1  $\rightarrow$  V4 (d) during attention to the contralateral hemifield (light  
 140 shading) and to the ipsilateral hemifield (dark shading), averaged over all site pairs then averaged over monkeys  
 141 after alignment to their beta and gamma peak frequencies. Same statistics conventions as a and b. (e, f)  
 142 Bidirectional GC influences for 7A  $\rightarrow$  V1 (l) and V1  $\rightarrow$  V4 (n), averaged over all site pairs then averaged over monkeys  
 143 after alignment to their beta and gamma peak frequencies. For 7A-V1, top-down influences are shown in blue  
 144 shading, and bottom-up influences in dark shading. For V1-V4, bottom-up influences are shown in green shading,  
 145 and top-down influences in light shading. Same statistical conventions as a and b, but with the statistical  
 146 distribution based on a non-parametric bootstrap procedure. (g) Top-down modulatory stream (blue arrow) from  
 147 7A  $\rightarrow$  V1, and bottom-up feedforward path from V1  $\rightarrow$  V4 (green arrow).

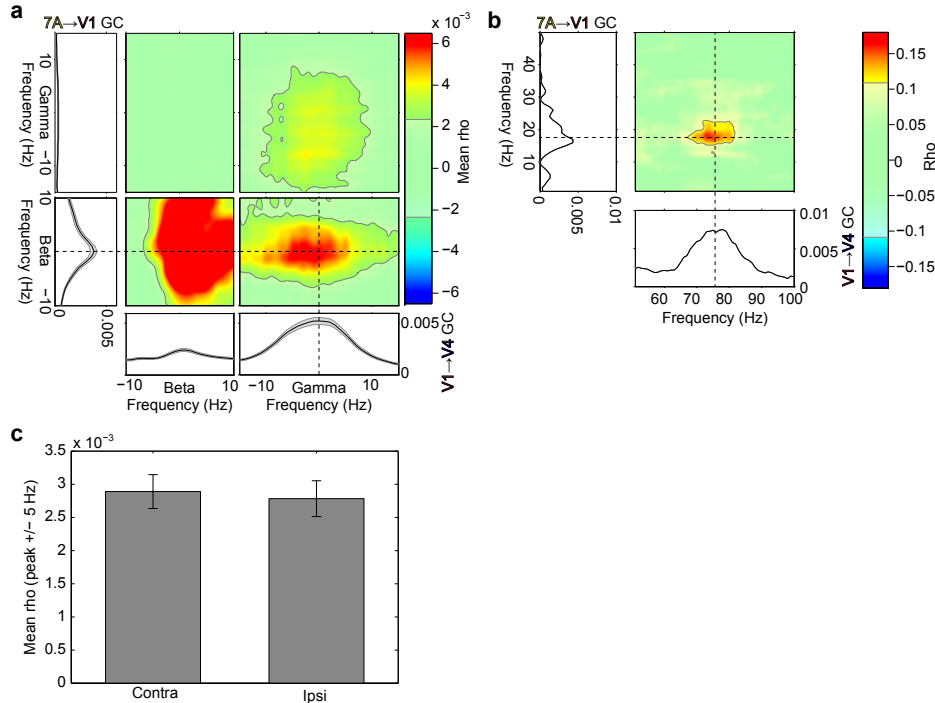
148

## 149 Top-down Beta Influences and Bottom-up Gamma Influences are Correlated Across 150 Time

151 Endogenous increases in top-down beta GC may lead to an increase in stimulus-driven bottom-up  
152 gamma GC; therefore, we sought to determine whether the observed top-down beta GC and bottom-  
153 up gamma GC are consistent with such a scenario. Quantification of correlation between moment-by-  
154 moment co-fluctuations in two GC influences is normally precluded by the fact that GC influences are  
155 not defined per single data epoch (without substantially sacrificing spectral resolution and/or signal-to-  
156 noise ratio). To surmount this problem, we used the recently developed method of Jackknife  
157 Correlation (JC), which quantifies the correlation by first calculating GC influences for all leave-one-out  
158 subsamples (i.e. the jackknife replications of all epochs) and then correlating these values (Richter,  
159 Thompson, Bosman, & Fries, 2015).

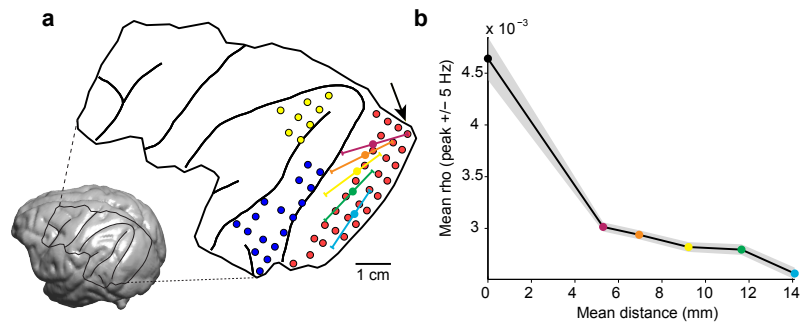
160 Here we used JC to correlate the top-down GC from a 7A site to a V1 site with the bottom-up GC from  
161 the same V1 site to a V4 site. We refer to these configurations of three sites as 'triplets', and the JC  
162 was determined for all possible 7A→V1→V4 triplets (N=10664, Monkey K: 3944, Monkey P=6720).  
163 The JC was calculated between all possible combinations of top-down frequencies and bottom-up  
164 frequencies, both ranging from 1-100 Hz. **Fig. 4a** shows the average over all triplets from each  
165 monkey averaged after alignment of their respective beta and gamma GC peaks. It reveals that top-  
166 down beta GC is correlated with bottom-up beta GC, and the same holds for the respective gamma  
167 GCs to a lesser extent. Crucially, top-down beta GC also shows a significant positive correlation with  
168 bottom-up gamma GC. The peak of this cross-frequency interaction is well aligned with the average  
169 7A→V1 beta and V1→V4 gamma GC peak frequencies (**Fig. 4a**, line plots – intersection of the  
170 dashed lines). Importantly, there is no significant JC between 7A→V1 gamma and V1→V4 beta GC,  
171 even though 7A→V1 gamma GC is significantly correlated to V1→V4 gamma GC and 7A→V1 beta  
172 GC is significantly correlated to V1→V4 beta GC. **Fig. 4b** shows a specific triplet selected from  
173 monkey K with a sizeable correlation coefficient of  $\rho(2653) = 0.16$  between 7A→V1 beta and  
174 V1→V4 gamma GC. Again, the area of maximal correlation is well aligned with the top-down beta and  
175 bottom-up gamma peak frequencies for this particular triplet. Thus, though the average level of  
176 correlation across triplets is relatively low, specific triplet correlations may fall between small to  
177 moderate size (Cohen, 1988). We tested for differences in the correlation coefficient between top-  
178 down beta and bottom-up gamma GC for the contralateral and ipsilateral conditions separately (**Fig.**  
179 **4c**). There was no significant difference between these conditions, consistent with a mechanism that  
180 exists under both attention conditions, such that attentional increases in top-down beta-band  
181 influences, as shown above, lead to increased bottom-up gamma-band influences, as we also show.

182 We next investigated whether the JC between 7A→V1 beta and V1→V4 gamma GC depended on  
183 involving the same V1 site, which would demonstrate spatial specificity at the level of recording sites.  
184 We tested this spatial specificity by pairing 7A→V1 beta GC to a specific V1 site, with V1→V4 gamma  
185 GC from a different V1 site, where the distance that separated the two V1 sites was parametrically  
186 varied. **Fig. 5a** shows for monkey K the boundaries of the recording grid and prominent sulci based on  
187 the monkey's MRI and surgical photographs. For each V1 site, 5 sets of other V1 sites were defined  
188 that fell into pre-specified distance intervals (1 cm per interval, stepped by 2.5 mm, between 0 and  
189 2 cm). **Fig. 5a** shows one example V1 site (arrow) and illustrates with 5 colored lines the five distance  
190 intervals (colored lines were slightly displaced for illustration purposes). The mean V1 distance for  
191 each distance interval is marked with a filled circle. **Fig. 5b** shows the resulting JC computed for a  $\pm 5$   
192 Hz frequency window around the peak 7A→V1 beta and V1→V4 gamma GC frequencies averaged  
193 over triplets and monkeys. It can be seen that as the distance between the two V1 sites increases  
194 from zero, there is a monotonic falloff of the correlation coefficient between 7A→V1 beta and V1→V4  
195 gamma GC. This indicates that top-down beta and bottom-up gamma GC influences are not global,  
196 but rather are spatially specific, such that the correlation is maximal when the top-down beta GC  
197 influence is targeting the same V1 region that is projecting the bottom-up gamma GC influence. This is



198

199 **Figure 4** Jackknife correlation. (a) The 4 colored panels show JC averaged over all 7A→V1→V4 triplets for each  
 200 monkey then averaged over both monkeys after aligning to the beta and gamma GC peak frequencies. The  
 201 frequencies of 7A→V1 GC are shown on the vertical axis, the frequencies of V1→V4 GC are shown on the  
 202 horizontal axis. The frequency ranges 1-50 Hz and 51-100 Hz are shown separately, because they required  
 203 slightly different spectral analyses (see Experimental Procedures). Non-significant regions are partially masked by  
 204 white ( $p > 0.01$ , two-tailed non-parametric randomization test, corrected for multiple comparisons across both  
 205 frequency axes). The line plots at the bottom show the GC spectra ( $\pm 1$  SEM) averaged over all V1→V4 site pairs.  
 206 The line plots to the left show the GC spectra ( $\pm 1$  SEM) averaged over all 7A→V1 site pairs. Dashed lines mark  
 207 the top-down beta GC spectral peak and the bottom-up gamma GC spectral peak. (b) Same as lower right color-  
 208 panel in a, but for an example triplet from monkey K showing a strong JC between 7A→V1 GC and V1→V4 GC.  
 209 As in a, dashed lines mark the GC spectral peaks. Due to more noisy spectra for this single example, peaks were  
 210 found by a specialized algorithm (findpeaksG.m by T.C O'Haver). (c) Average correlation coefficient at the top-  
 211 down beta and bottom-up gamma peaks ( $\pm 5$  Hz), as shown at the cross-hair in the lower right panel of a,  
 212 computed separately for contralateral and ipsilateral attention conditions. The difference is not statistically  
 213 significant ( $p = 0.77$ , two-tailed non-parametric randomization test).



214

215 **Figure 5** Spatial specificity of correlation between top-down beta and bottom-up gamma GC. (a) Inset: MRI of  
216 monkey K with the surgical trepanation and prominent sulci overlaid. The blow-up shows recording sites in 7A  
217 (yellow), V1 (red), and V4 (blue) that were analyzed. The V1 site marked by the arrow serves as an example to  
218 demonstrate the distance intervals from which another V1 site may have been chosen, which were 0 to 1 cm  
219 (magenta), 0.25 to 1.25 cm (orange), 0.5 to 1.5 cm (yellow), 0.75 to 1.75 cm (green), and 1 to 2 cm (cyan). Solid  
220 circles mark the average distance between V1 sites that were chosen for each distance interval. The particular  
221 arrangement of the distance intervals was chosen solely for the purpose of illustration. (b) Average jackknife  
222 correlation over a  $\pm 5$  Hz window around the top-down beta and bottom-up gamma GC peak frequencies,  
223 averaged over triplets, and monkeys. The solid black circle shows the result for triplets, i.e. where the top-down  
224 beta and bottom-up gamma GC influences are connected through the same V1 site. As the distance between V1  
225 sites increases, there is a monotonic falloff in the correlation coefficient. The mean distance between V1 sites is  
226 color-coded as solid circles matching the mean distances of the five distance intervals shown in a.

227 not trivially explained by GC calculation using the same V1 site, as explained in more detail in the  
228 discussion section.

## 229 Top-down Beta Influences Lead Bottom-up Gamma Influences in Time

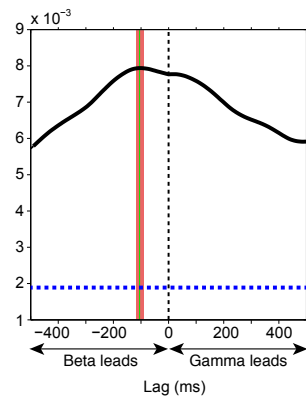
230 We have established that spontaneous fluctuations in endogenous top-down beta GC are correlated  
231 with fluctuations in stimulus-driven bottom-up gamma GC. To investigate whether the data contain  
232 evidence in support of a causal relation, we assessed whether top-down beta GC is predictive of  
233 subsequent bottom-up gamma GC. To accomplish this, we extended the JC by adding a temporal  
234 dimension not dissimilar from time-lagged cross-correlation. We compute the JC on time-frequency  
235 data, where we systematically offset the data by positive or negative lags. We call this procedure  
236 lagged jackknife correlation (LJC). This quantifies at what time delay between the top-down beta-band  
237 influence and the bottom-up gamma-band influence the JC between them is largest. We computed  
238 LJC for each triplet. **Fig. 6** shows the LJC averaged over triplets and monkeys and exhibits a peak at -  
239 0.105 s indicating that top-down beta GC leads bottom-up gamma GC by 0.105 s ( $t(10663) = -7.576$ ,  
240  $p < 0.001$ , two-tailed jackknife-based t-test).

## 241 DISCUSSION

242 We used LFP recordings from 252-channel ECoG arrays covering large parts of the left hemispheres  
243 of two macaques to analyze the interaction between top-down and bottom-up GC influences. Top-  
244 down influences were quantified between area 7a at the top of the visual hierarchy (Bastos, Vezoli, et  
245 al., 2015b; Markov et al., 2014) and V1 at the bottom. Bottom-up GC influences were quantified  
246 between V1 and V4, a known feedforward pathway carrying stimulus driven input (Bosman et al.,  
247 2012). Inter-areal top-down influences showed a beta-band peak, that was independent of visual  
248 stimulation and therefore endogenously generated, that was significantly larger in the top-down than  
249 the bottom-up direction, and that increased with selective attention. Bottom-up influences showed a  
250 gamma-band peak, that was stimulus driven, that was significantly larger in the bottom-up than the  
251 top-down direction, and that also increased with selective attention. Jackknife Correlation between top-  
252 down beta-band influences and bottom-up gamma-band influences revealed a cross-frequency  
253 interaction. This interaction was spatially specific, as it was maximal between top-down and bottom-up  
254 inter-areal influences that shared the same V1 site. Finally, top-down beta-band influences best  
255 predicted bottom-up gamma-band influences ~100 ms later, suggesting that the cross-frequency  
256 interaction is causal.

257 There are potential concerns related to the influence of noise. Noise can affect GC and it could  
258 thereby in principle affect the JC between GC fluctuations that we analyze here. One relevant scenario  
259 concerns noise that is shared between two signals, which can lead to artifactual GC (Nalatore et al.,  
260 2007; Vinck et al., 2015). Shared noise is typically due to volume conduction, which is strongly  
261 attenuated in our signals due to the bipolar derivation (Trongnetrpunya et al., 2015). Furthermore,  
262 artifactual GC alone does not lead to JC between GC, because the latter requires correlated GC  
263 fluctuations. GC fluctuations could in principle be due to fluctuations in shared noise. However, such  
264 noise influences on the two GC metrics would occur simultaneously and therefore, the lagged JC  
265 would peak at zero lag, whereas we found a lag of ~100 ms. Other influences of noise can be  
266 envisaged, and with sufficiently complex assumptions on multiple noise sources, essentially any  
267 correlation can be explained. The set of observations presented here, namely the fact that GC is  
268 correlated between different frequency bands, that this correlation shows high spatial specificity and in  
269 particular that the peak correlation occurs at a lag, would require assumptions that appear extremely  
270 implausible.

271 Whereas noise is unlikely to explain the overall pattern of results, it might well influence the magnitude  
272 of observed correlations. The magnitude of correlations might be relevant to assess their functional  
273 significance. The JC for some triplets was at the level of  $\rho \approx 0.2$ , i.e. of moderate strength. However,  
274 the mean JC over all triplets tended towards a value an order of magnitude lower. This relatively low



275  
276 **Figure 6** Lagged jackknife correlation (LJC) analysis. (a) Average LJC across triplets at the top-down beta and  
277 bottom-up gamma peak GC frequencies for each monkey, then averaged over monkeys for a  $\pm 0.5$  s lag. The  
278 blue dashed line denotes the significance level ( $p=0.05$ , two-tailed non-parametric randomization test) of the LJC.  
279 A dashed black line is drawn at zero lag. The green vertical line indicates the lag of the maximum LJC value, with  
280  $\pm 1$  SEM in red. The lag of the peak LJC value is significantly different from zero ( $t(10663) = -7.576$ ,  $p < 0.001$ ,  
281 two-tailed).  
282

283 magnitude might be explained by uncorrelated noise. Uncorrelated physiological, measurement, and  
284 estimation noise will invariably lead to an underestimation of the true JC. These detrimental effects of  
285 noise are maximal for short data epochs and for correlations based on single trials, i.e. JC. Short data  
286 epochs, necessary to capture rapid fluctuations as the basis of our JC and LJC results, do not provide  
287 for the averaging out of stochastic physiological or measurement noise (Richter et al. (2015). JC  
288 across single trials, necessary for maximal sensitivity and fidelity, similarly reduces the correlation  
289 magnitude as compared to alternative approaches like sorting-and-binning that artificially inflate  
290 correlation magnitude (Richter et al. (2015).

291 Numerous studies in visual cortex have reported gamma-band synchronization within and between  
292 visual areas (Bichot, Rossi, & Desimone, 2005; Engel, Kreiter, König, & Singer, 1991; Fries, 2001;  
293 Fries, Roelfsema, Engel, König, & Singer, 1997; Gray & Singer, 1989; Hoogenboom, Schoffelen,  
294 Oostenveld, Parkes, & Fries, 2006; Kreiter & Singer, 1996; Tallon-Baudry, Bertrand, Delpuech, &  
295 Pernier, 1996; Taylor, Mandon, Freiwald, & Kreiter, 2005; Womelsdorf, Fries, Mitra, & Desimone,  
296 2006; Wyart & Tallon-Baudry, 2008), and numerous studies in parietal cortex have reported beta-band  
297 synchronization within parietal areas and between parietal and frontal areas (Buschman & Miller,  
298 2007; Dotson, Salazar, & Gray, 2014; Salazar, Dotson, Bressler, & Gray, 2012; Stetson & Andersen,  
299 2014). Recent ECoG recordings covering both visual and parietal areas revealed that inter-areal beta-  
300 band influences predominate in the top-down and inter-areal gamma-band influences predominate in  
301 the bottom-up direction (Bastos, Vezoli, et al., 2015b). These findings link parietal beta-band activity  
302 with visual gamma-band activity and suggest a concrete case of cross-frequency interaction (Bressler  
303 & Richter, 2015). In the present paper, we have tested some of the resulting predictions and found  
304 direct experimental support for such a cross-frequency interaction that allows top-down beta-band  
305 influences to enhance bottom-up gamma-band influences.

306 Cortical anatomy has revealed a distinct laminar pattern of top-down and bottom-up projections  
307 (Felleman & Van Essen, 1991; Markov et al., 2014). Bottom-up projections originate predominantly in  
308 superficial layers, and this predominance increases with the number of hierarchical levels bridged by  
309 the bottom-up projection. Furthermore, bottom-up projections terminate predominantly in layer 4. Top-  
310 down projections originate predominantly in deep layers, and this predominance increases with the  
311 number of hierarchical levels bridged by the top-down projection. Furthermore, top-down projections  
312 terminate predominantly outside layer 4, primarily in layers 1 and 6. Determining how the respective  
313 top-down influences interact with local processing and thereby ultimately with bottom-up influences  
314 remains a central neuroscientific quest. One potential mechanism has been proposed in a model that  
315 entails details of both layer-specific anatomy and cellular biophysics (Lee, Whittington, & Kopell,  
316 2013), and that replicates effects of top-down selective attention on bottom-up gamma-band  
317 coherence. The model implicates a subclass of inhibitory interneurons, the slow-inhibitory (SI)  
318 interneurons, as targets of top-down modulation. These cells may span multiple cortical laminae and  
319 thus are suitably situated for integration of neuronal activity across layers. A subpopulation of these  
320 cells, low-threshold spiking (LTS) cells, are found in deep layers of the cortex and are: 1) hypothesized  
321 to receive top-down input, 2) implicated in the generation of beta oscillations and in the resonant  
322 response to beta-rhythmic top-down input and 3) selectively modulate gamma band activation in layer  
323 2/3, leading to an enhanced gamma band output. Our present analysis confirms the central prediction  
324 of the Lee et al. (2013) paper, namely that specifically top-down beta-band influences enhance  
325 stimulus-driven gamma-band processes. Lee et al. show how this mechanism can support the  
326 implementation of attentional stimulus selection. The current results, which mechanistically link the  
327 previously reported attentional enhancements of top-down beta and bottom-up gamma influences,  
328 provide the hitherto missing experimental bridge. Together, experiments, modeling and model-testing  
329 data analysis have led to an intriguingly coherent understanding of the neuronal processes behind the  
330 implementation of attentional stimulus selection.

## 331 METHODS

### 332 Visual Stimulation and Behavioral Task

333 The experiment was approved by the ethics committee of the Radboud University Nijmegen  
334 (Nijmegen, The Netherlands). Two adult male macaque monkeys (monkey K and monkey P, both  
335 macaca mulatta) were used in this study. During experiments, monkeys were placed in a dimly lit  
336 booth facing a CRT monitor (120 Hz non-interlaced). When they touched a bar, a fixation point was  
337 presented, and gaze had to remain within the fixation window throughout the trial (monkey K: 0.85 deg  
338 radius, monkey P: 1 deg radius), otherwise the trial would be terminated and a new trial would  
339 commence. Once central fixation had been achieved and a subsequent 0.8 s pre-stimulus interval had  
340 elapsed, two isoluminant and isoeccentric drifting sinusoidal gratings were presented, one in each  
341 visual hemifield (diameter: 3 deg, spatial frequency: ~1 cycle/deg, drift velocity: ~1 deg/s, resulting  
342 temporal frequency: ~1 cycle/s, contrast: 100%). Blue and yellow tints were randomly assigned to  
343 each of the gratings on each trial (**Fig. 1a**). Following a random delay interval (monkey K : 1 - 1.5 s;  
344 monkey P : 0.8 - 1.3 s), the central fixation point changed color to match one of the drifting gratings,  
345 indicating that this grating was the target stimulus, i.e. the fixation point color was the attentional cue.  
346 When the target stimulus was positioned in the visual hemifield contralateral to the recorded  
347 hemisphere, we refer to this condition as attend contra, whereas when the target was in the ipsilateral  
348 hemifield with respect to the ECoG grid, this condition is labeled attend ipsi. Either the target or  
349 distracter stimulus could undergo a subtle change in shape consisting of a transient bending of the  
350 bars of the grating (0.15 s duration of the full bending cycle). This change could occur at any monitor  
351 refresh from 0.75 s to 5 s (monkey K), and 4 s (monkey P) after stimulus onset. Bar releases within  
352 0.15 - 0.5 s after target changes were rewarded. If stimulus changes occurred before the cue indicated  
353 which stimulus was the target, reports were rewarded in a random half of trials. Bar releases after  
354 distracter changes terminated the trial without reward. Trials were pooled from both contra and ipsi  
355 conditions, except where explicit comparisons of these conditions were made.

### 356 Neurophysiological Recordings

357 LFP recordings were made via a 252 channel electrocorticographic grid (ECoG) implanted subdurally  
358 over the left hemisphere (Rubehn, Bosman, Oostenveld, Fries, & Stieglitz, 2009). Data from the same  
359 animals, partly overlapping with the data used here, have been used in several previous studies  
360 (Bastos, Litvak, et al., 2015a; Bastos, Vezoli, et al., 2015b; Bosman et al., 2012; Brunet et al., 2014;  
361 2015; Lewis, Bosman, Womelsdorf, & Fries, 2016; Pinotsis et al., 2014; Richter et al., 2015).  
362 Recordings were sampled at approximately 32 kHz with a passband of 0.159 – 8000 Hz using a  
363 Neuralynx Digital Lynx system. The raw recordings were low-pass filtered to 250 Hz, and  
364 downsampled to 1 kHz. The electrodes were distributed over eight 32-channel headstages, and  
365 referenced against a silver wire implanted onto the dura overlying the opposite hemisphere. The  
366 electrodes were re-referenced via a bipolar scheme to achieve 1) greater signal localization 2)  
367 cancellation of the common reference, which could corrupt the validity of connectivity metrics, 3) to  
368 reject headstage specific noise. The bipolar derivation scheme subtracted the recordings from  
369 neighboring electrodes (spaced 2.5 mm) that shared a headstage, resulting in 218 bipolar derivations,  
370 henceforth referred to as “sites” (see Bastos et al. (2015b) for a detailed discussion of the re-  
371 referencing procedure). The site locations are shown as spheres in **Fig. 1b** (monkey K: white, monkey  
372 P: black).

373 Three ROIs were selected for the current study: V1, V4, and area 7A (referred to simply as “7A”). ROIs  
374 were defined based on comparison of the electrode locations (co-registered to each monkey’s  
375 anatomical MRI and warped to the F99 template brain in CARET (Van Essen, 2012), with multiple  
376 cortical atlases of the macaque (see Bastos et al. (2015b) for a detailed discussion). Recording sites  
377 composing each ROI were co-registered to a common template (INIA19, (Rohlfing et al., 2012)), as  
378 were the Paxinos ROI definitions (Paxinos, Huang, & Toga, 1999). The V1/V2 combined definition of

379 Paxinos et al. (1999), is shown in **Fig. 1b, 3g** (red) for simplicity due to uncertainty across atlases of  
380 the V1/V2 border, though recording site selection was based on multiple atlases with no recording  
381 sites selected that were believed to belong to area V2. Based on these ROI definitions, 77 recording  
382 sites were selected from area V1 (monkey K: 29, monkey P: 48), 31 from area V4 (monkey K: 17,  
383 monkey P: 14), and 18 from area 7A (monkey K: 8, monkey P: 10).

## 384 Preprocessing and Spectral Analysis General

385 Signal processing was conducted using the FieldTrip toolbox (Oostenveld, Fries, Maris, & Schoffelen,  
386 2011). The raw data was line noise rejected via the subtraction of 50, 100, and 150 Hz components fit  
387 to the data using a discrete Fourier transform. Following trial epoching, specific to each analysis,  
388 epochs for each site were de-meant. Epochs exceeding 5 standard deviations of all data from the  
389 same site in the same session were rejected. In addition, epochs were manually inspected and epochs  
390 with artifacts were rejected. The remaining epochs were normalized by the variance across all data in  
391 all epochs from the same site in the same recording session. Subsequently, all epochs were combined  
392 across sessions.

393 Spectral analysis was performed via the fast Fourier transform (FFT) on 0.5 s epochs. For frequencies  
394 from 0-50 Hz, a Hann taper was utilized, whereas for frequencies above 50 Hz, the multitaper method  
395 (MTM) was used to improve the spectral concentration of the gamma rhythm (Percival & Walden,  
396 1993; Thomson, 1982). We applied 5 tapers, resulting in a spectral smoothing of +/- 6 Hz. All epochs  
397 were zero-padded to 1 s resulting in a spectral resolution of 1 Hz. The coefficients resulting from the  
398 FFT were used to determine the cross spectral density, which is the basis for two connectivity metrics  
399 employed: pairwise phase consistency (PPC) (Vinck et al., 2010), and Granger causality (GC)  
400 (Bressler & Seth, 2011; Granger, 1969). When GC is computed from the cross-spectral density, this is  
401 known as a non-parametric approach in contrast to the traditional parametric method based on  
402 autoregressive modeling (Dhamala, Rangarajan, & Ding, 2008). Connectivity metrics were computed  
403 between all inter-areal pairings of sites between ROIs: V1-V4, and V1-7A.

## 404 High Resolution Spectral Comparisons

405 For the analyses of **Fig. 2** and **Fig. 3**, we used all 0.5 s epochs that could be defined with 60%  
406 overlap. This overlap allows for the application of Welch's method (Welch, 1967) and was selected as  
407 an optimal overlap for the multitaper method, while maintaining a reasonable computational load  
408 (Percival & Walden, 1993; Thomson, 1977) For the analysis of stimulation and fixation periods, each  
409 trial was segmented into a fixation and stimulation segment. The fixation period was defined as the 0.5  
410 s prior to stimulus onset, while the stimulation period was defined from 0.3 s post-stimulus onset (to  
411 avoid onset related transients) until the first of three possible events 1) the onset of the cue, 2) a  
412 change in the distracter stimulus, or 3) a change in the target stimulus. This resulted in 6822 fixation  
413 epochs (Monkey K: 3384, Monkey P: 3438) and 13675 stimulation epochs (Monkey K: 8109, Monkey  
414 P: 5566). PSDs (**Fig. 2a-f**) were divided by  $1/f$  to reduce the  $1/f$  component. Fixation versus stimulation  
415 was only compared for PPC, which inherently controls for sample size bias, thus no adjustments  
416 needed to be made to the large disparity in the number of trials between the fixation and stimulation  
417 conditions. Statistical assessment of the within-subject difference between fixation and stimulation  
418 conditions employed a non-parametric technique (Maris & Oostenveld, 2007) that inherently controls  
419 for multiple comparisons, where epochs were pooled and then randomly distributed between the  
420 fixation and stimulation conditions. FFT was then performed, followed by PPC. The difference between  
421 conditions was then computed, with the maximum absolute difference across the frequencies retained.  
422 This critical step ensures that the statistical test is corrected for multiple comparisons across the  
423 frequency dimension. The procedure was repeated 1000 times, forming a distribution of surrogate  
424 values against which the empirical values at each frequency may be compared. Group statistics were  
425 performed on the peak-aligned data by first averaging over all site pairs within-subject, and then  
426 averaging these results across the monkeys. This ensured that each monkey contributed equally to  
427 the overall result, despite having different numbers of site pairs. This averaging procedure was

428 performed for each permutation, followed by the same max-based multiple-comparison correction.  
429 This gives rise to a surrogate distribution of data against which the group data may be assessed.  
430 Multiple comparisons correction was performed across all frequencies tested (1-45 Hz and 55-100 Hz  
431 in steps of 1 Hz).

432 To compare attention to the hemifield contralateral (“attend contra”) versus ipsilateral (“attend ipsi”) to  
433 the recorded hemisphere, we defined the post-cue period as the time from 0.3 s after cue presentation  
434 (to avoid cue presentation transients) until the first change in either the target or distracter stimulus.  
435 This period was segmented into as many 0.5 s epochs as possible with 60 % overlap. This resulted in  
436 8313 attend contra epochs (Monkey K: 3819, Monkey P: 4494) and 7899 attend ipsi epochs (Monkey  
437 K: 3456, Monkey P: 4443), i.e. a total of 16212 attend epochs (Monkey K: 7275, Monkey P: 8937).  
438 Non-parametric GC is known to be biased by sample size (Bastos & Schoffelen, 2015), thus the  
439 number of epochs per attention condition needed to be balanced for each monkey. This was  
440 accomplished by finding the condition with the fewest epochs, and randomly selecting this number of  
441 epochs from the other condition. The statistical difference between conditions was also assessed  
442 using a non-parametric statistical framework as described for the fixation versus stimulation contrast.

443 The comparison of top-down versus bottom-up GC was performed on the pooled data from the attend  
444 contra and ipsi conditions. Since this was a within-condition comparison, no balancing of epoch  
445 numbers was needed, and all epochs from both attend conditions were used. The statistical analysis  
446 of the difference between top-down and bottom-up GC could not be obtained using a non-parametric  
447 randomization framework, because top-down and bottom-up GC are not properties of specific sets of  
448 epochs, but rather are expressed by all trials simultaneously. Therefore, an alternative statistical  
449 approach was used, namely the bootstrap (Efron & Tibshirani, 1994). Like with the randomization  
450 approach, the statistic of interest – in this case the top-down/bottom-up GC difference – is recomputed  
451 on each bootstrap resample, giving rise to a distribution of surrogate values. Following Efron and  
452 Tibshirani (1994), a confidence interval can be constructed from the surrogate distribution. To assess  
453 the statistical significance at  $p=0.05$  (two-tailed), we find the 2.5<sup>th</sup> and 97.5<sup>th</sup> percentile values from the  
454 surrogate distribution of differences between top-down and bottom-up GC. This naturally forms the  
455 95% confidence interval such that if zero lies outside of this interval, we may conclude that the result is  
456 significant at a level of  $p=0.05$ . This method does not control for multiple comparisons, but we can  
457 easily modify it to do so using the same logic employed by Maris and Oostenveld (2007). We  
458 performed 1000 bootstrap resamples. For each resample we determined the absolute difference  
459 across frequencies between the bootstrap resample spectrum and the average of all bootstrap  
460 resamples, and retained the maximum of this value across frequencies. Thus we are guaranteed to  
461 form the largest confidence interval possible across frequencies and in so doing construct an omnibus  
462 confidence interval that controls for the multiple comparisons. This confidence interval is applied to  
463 each frequency, and where it does not contain zero, the result is significant at  $p=0.05$ . To conduct  
464 group level statistics, the omnibus statistic is derived from the mean of each bootstrap resample of the  
465 difference between top-down and bottom-up spectra across both monkeys (first averaged within-  
466 subject across pairs), such that the mean of the empirical difference across the monkeys can be  
467 assessed for significance.

## 468 Jackknife Correlation

469 We aimed at quantifying the correlation between moment-by-moment co-fluctuations in two GC  
470 influences. This is normally precluded by the fact that GC influences are not defined per single data  
471 epoch (without substantially sacrificing spectral resolution and/or signal-to-noise ratio). Therefore, we  
472 used the Jackknife Correlation (JC), which quantifies the correlation by first calculating GC influences  
473 for all leave-one-out subsamples (i.e. the jackknife replications of all epochs) and then correlating  
474 these values (Richter et al., 2015). For each leave-one-out subsample, the GC or any other smooth  
475 function  $F$  of the data can be defined as follows:

476

$$F_{x_j} = F(x_1, x_2, \dots, x_{j-1}, x_{j+1}, \dots, x_n) \quad (1)$$

477

478 , where  $x$  specifies the recording site and  $j$  specifies the index of the left-out observation, here the  
479 epoch. JC requires independent epochs. Thus, we followed the same segmentation strategy as for the  
480 comparison of the attend conditions, but with zero overlap, which resulted in fewer epochs, totaling  
481 6414 (Monkey K: 2655, Monkey P: 3759). Contra and ipsi conditions were combined for the JC  
482 analysis. The JC is defined using the following formula:

483

$$JC_{F_x F_y} = \frac{1}{n-1} \sum_{j=1}^n \left( \frac{F_{x_j} - \bar{F}_x}{s_{F_x}} \right) \left( \frac{F_{y_j} - \bar{F}_y}{s_{F_y}} \right) \quad (2)$$

484

485 , where  $n$  is defined as the number of jackknife replications and is equal to the total number of epochs,  
486  $F_{x_j}$  and  $F_{y_j}$  are the jackknife replications,  $\bar{F}_x$  and  $\bar{F}_y$  are the means of the jackknife replications, and  $s_{F_x}$   
487 and  $s_{F_y}$  are the standard deviations of the jackknife replications. To use the JC with the Spearman  
488 correlation metric, we applied the above formula on the ranks of  $F_{x_j}$  and  $F_{y_j}$ .

489 For statistical testing, we created a distribution of 1000 JC values under a realization of the null  
490 hypothesis of independence between 7A→V1 and V1→V4 GC influences. This was realized by  
491 calculating JC between randomly permuted jackknife replications of 7A→V1 and V1→V4 GC  
492 influences. This is equivalent to calculating the JC between GC influences after leaving out a random  
493 epoch for the 7A→V1 GC and a random epoch for the V1→V4 GC without replacement. To control for  
494 multiple comparisons across the frequency-frequency combinations, the max-based approach (see  
495 above) was again employed, where for each permutation the maximum absolute Spearman's rho  
496 value was selected, giving rise to an omnibus distribution of surrogate correlation coefficients for each  
497 triplet. For maps showing the average correlation across triplets, this max-based method was  
498 performed on the mean over triplets, where for a given permutation each triplet was randomized in the  
499 same order as all others. This was done individually per monkey and after averaging across the two  
500 monkeys. When monkeys were combined, spectra were aligned to the beta- and gamma-peak  
501 frequencies and averages were first taken across all triplets of each monkey to weight both monkeys  
502 equally.

503 For testing spatial specificity, we analyzed recording site triplets, which did not share the same V1 site  
504 (see main text for details): 7A→V1<sub>a</sub>V1<sub>b</sub>→V4. Since a vast number of such triplets exist, yet we wished  
505 to select a number equal to the original number of triplets to control potential statistical bias, we  
506 selected a unique number of 7A→V1<sub>a</sub>V1<sub>b</sub>→V4 triplets that matched the original number of  
507 7A→V1→V4 triplets evaluated for each monkey and then the performed the same JC procedure. To  
508 smooth the result statistically (exploring the large space of possibilities), we repeated this procedure  
509 100 times, resulting in unique selections of V1 sites for each distance interval, and averaged the  
510 outcomes. Results were plotted against the average distance obtained for each distance interval.

### 511 Lagged Jackknife Correlation (LJC)

512 We used the jackknife correlation (JC) to quantify the correlation between top-down beta GC and  
513 bottom-up gamma GC. To this end, we left out one data epoch at a time, calculated GC influences,  
514 and determined the correlation between the resulting GC influences across all leave-one-out  
515 (jackknife) replications. Since a given jackknife replication eliminated the same epoch for the  
516 calculation of both GC influences, this established the correlation at zero time lag. Next, we were  
517 interested in whether the correlation depends on the time lag. To test this, we computed JC between  
518 GC influences calculated from epochs offset by a variable lag. The epochs were stepped at  $t$  intervals

519 of 5 ms. The offsets were stepped at  $\tau$  intervals of 5 ms. Note that stepping of intervals and offsets  
 520 was in principle independent and could have been different, but it was chosen to be identical to speed  
 521 up computation. We refer to this as lagged JC (LJC):

522

$$LJC_{F_x F_y}(\tau) = \frac{1}{n-1} \sum_{j=1}^n \left( \frac{F_{x_{j,t}} - \bar{F}_x}{S_{F_{x_t}}} \right) \left( \frac{F_{y_{j,t+\tau}} - \bar{F}_y}{S_{F_{y_{t+\tau}}}} \right) \quad (3)$$

523

524  $\tau$  was chosen to cover a range of lags from -500 ms to 500 ms. The GC calculation itself was as in the  
 525 previous zero-lag JC, using 500 ms and the tapering specified above. We used data from 0.3 s post-  
 526 cue to 2 s post-cue, eliminating shorter trials so that longer lags could be tested (878 trials used,  
 527 Monkey K: 398, Monkey P: 480). LJC was calculated across trials, i.e. leaving out an entire trial at a  
 528 time (this is different from the previous zero-lag JC, which used multiple non-overlapping epochs per  
 529 trial if available). The data that was available per trial allowed for multiple realizations of the two  
 530 epochs with a particular lag. For each lag, LJC was calculated separately for all possible realizations  
 531 and averaged. The number of possible realizations decreases as the lag between top-down beta GC  
 532 and bottom-up gamma GC increases, resulting in fewer LJC computations that are averaged. This  
 533 results in a noisier estimate at larger lags, but no systematic bias in the mean JC value. The number of  
 534 epochs that each LJC is computed upon always equals the number of trials. Formally, this  
 535 implementation of the LJC is defined as:

536

$$LJC_{F_x F_y}(\tau) = \frac{1}{m-\tau} \sum_{t=1}^{m-\tau} \left[ \frac{1}{n-1} \sum_{j=1}^n \left( \frac{F_{x_{j,t}} - \bar{F}_{x_t}}{S_{F_{x_t}}} \right) \left( \frac{F_{y_{j,t+\tau}} - \bar{F}_{y_{t+\tau}}}{S_{F_{y_{t+\tau}}}} \right) \right] \quad (4)$$

537

538 , where  $m$  is the number of 500 ms windows, stepped at 5 ms, that fitted into the trial length of 1.7 s.

539 Statistical significance was assessed using the same logic as used for the JC, where the epoch order  
 540 of one member of the JC was permuted with respect to the other. For the LJC, the permutation was  
 541 identical for each time step and lag, to be conservative. Multiple comparison correction must take  
 542 place over the multiple lags, which is achieved by taking the maximum absolute Spearman's rho value  
 543 across lags for each permutation. The resulting distribution is used to assess the probability that the  
 544 empirical result at each lag occurred by chance. The empirical and the permutation metrics were first  
 545 averaged over all triplets per monkey and then averaged over the two monkeys, to give equal weight  
 546 to both subjects.

547 We wished to assess whether the LJC peak lag of -105 ms was significantly different from a lag of  
 548 zero. We did so using a jackknife method to determine the standard error of the peak position in  
 549 milliseconds (Efron, 1981). In this case we leave out a specific triplet to assess the variability of the  
 550 peak. The jackknife procedure causes a compression of the variance (Richter et al., 2015), thus the  
 551 5 ms sampling grid would not be sufficient to represent the peak positions of the jackknife replications.  
 552 To account for this, we cubic spline interpolated each replication to a resolution of 0.001 ms, which  
 553 proved adequate to represent the variance of the peak. The peak of each jackknife replication was  
 554 found using a Gaussian fit of the smoothed correlation as a function of lag (findpeaksG.m by T.C  
 555 O'Haver). We then derived the standard error of the estimator, and converted this to a t-score by  
 556 dividing the mean peak lag value of the jackknife replications by the estimated standard error. The  
 557 significance of this t-value was then assessed against Student's t-distribution. At the group level, this  
 558 procedure entails concatenating the data from both monkeys, and leaving out each triplet once. Based

559 on this group estimate of the standard error, a t-value is derived, as above, and assessed for statistical  
560 significance.

561

## 562 AUTHOR CONTRIBUTIONS

563 Conceptualization, C.G.R., W.H.T., C.A.B., and P.F.; Methodology, C.G.R., W.H.T., C.A.B., and P.F.;  
564 Software, C.G.R. and W.H.T.; Formal Analysis, C.G.R. and W.H.T.; Investigation, C.A.B. and P.F.;  
565 Writing – Original Draft, C.G.R. and P.F.; Writing – Review & Editing, C.G.R., W.H.T., C.A.B., and  
566 P.F.; Visualization, C.G.R.; Supervision, P.F.; Funding Acquisition, P.F.

## 567 ACKNOWLEDGMENTS

568 We would like to thank J. Vezoli for his assistance in ROI definition, co-registration and construction of  
569 anatomical renderings. This work was supported by DFG (SPP 1665, FOR 1847, FR2557/5-1-  
570 CORNET), EU (HEALTH-F2-2008-200728-BrainSynch, FP7-604102-HBP), a European Young  
571 Investigator Award, National Institutes of Health (1U54MH091657-WU-Minn-Consortium-HCP), the  
572 LOEWE program (NeFF) and an NWO-FLAG-ERA Joint Transnational Call 2015 (CAB).

## 573 REFERENCES

- 574 Bastos, A. M., & Schoffelen, J.-M. (2015). A Tutorial Review of Functional Connectivity  
575 Analysis Methods and Their Interpretational Pitfalls. *Frontiers in Systems Neuroscience*,  
576 9, 175. <http://doi.org/10.3389/fnsys.2015.00175>
- 577 Bastos, A. M., Litvak, V., Moran, R., Bosman, C. A., Fries, P., & Friston, K. J. (2015a). A  
578 DCM study of spectral asymmetries in feedforward and feedback connections between  
579 visual areas V1 and V4 in the monkey. *NeuroImage*, 108, 460–475.  
580 <http://doi.org/10.1016/j.neuroimage.2014.12.081>
- 581 Bastos, A. M., Usrey, W. M., Adams, R. A., Mangun, G. R., Fries, P., & Friston, K. J. (2012).  
582 Canonical microcircuits for predictive coding. *Neuron*, 76(4), 695–711.  
583 <http://doi.org/10.1016/j.neuron.2012.10.038>
- 584 Bastos, A. M., Vezoli, J., Bosman, C. A., Schoffelen, J.-M., Oostenveld, R., Dowdall, J. R., et  
585 al. (2015b). Visual areas exert feedforward and feedback influences through distinct  
586 frequency channels. *Neuron*, 85(2), 390–401.  
587 <http://doi.org/10.1016/j.neuron.2014.12.018>
- 588 Bichot, N. P., Rossi, A. F., & Desimone, R. (2005). Parallel and serial neural mechanisms for  
589 visual search in macaque area V4. *Science*, 308(5721), 529–534.  
590 <http://doi.org/10.1126/science.1109676>
- 591 Bieri, K. W., Bobbitt, K. N., & Colgin, L. L. (2014). Slow and fast  $\gamma$  rhythms coordinate  
592 different spatial coding modes in hippocampal place cells. *Neuron*, 82(3), 670–681.  
593 <http://doi.org/10.1016/j.neuron.2014.03.013>
- 594 Bosman, C. A., Schoffelen, J.-M., Brunet, N., Oostenveld, R., Bastos, A. M., Womelsdorf, T.,  
595 et al. (2012). Attentional Stimulus Selection through Selective Synchronization between  
596 Monkey Visual Areas. *Neuron*, 75(5), 875–888.  
597 <http://doi.org/10.1016/j.neuron.2012.06.037>
- 598 Bressler, S. L., & Richter, C. G. (2015). Interareal oscillatory synchronization in top-down  
599 neocortical processing. *Current Opinions in Neurobiology*, 31, 62–66.  
600 <http://doi.org/10.1016/j.conb.2014.08.010>
- 601 Bressler, S. L., & Seth, A. K. (2011). Wiener-Granger causality: a well established  
602 methodology. *NeuroImage*, 58(2), 323–329.  
603 <http://doi.org/10.1016/j.neuroimage.2010.02.059>
- 604 Brunet, N. M., Bosman, C. A., Vinck, M., Roberts, M., Oostenveld, R., Desimone, R., et al.  
605 (2014). Stimulus repetition modulates gamma-band synchronization in primate visual  
606 cortex. *Proceedings of the National Academy of Sciences of the United States of*  
607 *America*, 111(9), 3626–3631. <http://doi.org/10.1073/pnas.1309714111>
- 608 Brunet, N., Bosman, C. A., Roberts, M., Oostenveld, R., Womelsdorf, T., De Weerd, P., &  
609 Fries, P. (2015). Visual Cortical Gamma-Band Activity During Free Viewing of Natural  
610 Images. *Cereb Cortex*, 25(4), 918–926. <http://doi.org/10.1093/cercor/bht280>

- 611 Buschman, T. J., & Miller, E. K. (2007). Top-down versus bottom-up control of attention in  
612 the prefrontal and posterior parietal cortices. *Science*, *315*(5820), 1860–1862.  
613 <http://doi.org/10.1126/science.1138071>
- 614 Cohen, J. (1988). *Statistical Power Analysis for the Behavioral Sciences*. Lawrence Erlbaum  
615 Associates.
- 616 Colgin, L. L., Denninger, T., Fyhn, M., Hafting, T., Bonnevie, T., Jensen, O., et al. (2009).  
617 Frequency of gamma oscillations routes flow of information in the hippocampus. *Nature*,  
618 *462*(7271), 353–357. <http://doi.org/10.1038/nature08573>
- 619 Dhamala, M., Rangarajan, G., & Ding, M. (2008). Analyzing information flow in brain  
620 networks with nonparametric Granger causality. *NeuroImage*, *41*(2), 354–362.  
621 <http://doi.org/10.1016/j.neuroimage.2008.02.020>
- 622 Ding, M., Chen, Y., & Bressler, S. L. (2006). Granger Causality: Basic Theory and  
623 Application to Neuroscience. *Handbook of Time Series Analysis: Recent Theoretical*  
624 *Developments and Applications*. <http://doi.org/10.1002/9783527609970.ch17>
- 625 Dotson, N. M., Salazar, R. F., & Gray, C. M. (2014). Frontoparietal correlation dynamics  
626 reveal interplay between integration and segregation during visual working memory. *The*  
627 *Journal of Neuroscience : the Official Journal of the Society for Neuroscience*, *34*(41),  
628 13600–13613. <http://doi.org/10.1523/JNEUROSCI.1961-14.2014>
- 629 Efron, B. (1981). Nonparametric estimates of standard error: The jackknife, the bootstrap and  
630 other methods. *Biometrika*.
- 631 Efron, B., & Tibshirani, R. J. (1994). *An Introduction to the Bootstrap*. Boca Raton: CRC  
632 Press.
- 633 Engel, A. K., Kreiter, A. K., König, P., & Singer, W. (1991). Synchronization of oscillatory  
634 neuronal responses between striate and extrastriate visual cortical areas of the cat.  
635 *Proceedings of the National Academy of Sciences of the United States of America*,  
636 *88*(14), 6048–6052.
- 637 Felleman, D., & Van Essen, D. C. (1991). Distributed hierarchical processing in the primate  
638 cerebral cortex. *Cerebral Cortex*, *1*(1), 1–47.
- 639 Fontolan, L., Morillon, B., Liegeois-Chauvel, C., & Giraud, A.-L. (2014). The contribution of  
640 frequency-specific activity to hierarchical information processing in the human auditory  
641 cortex. *Nature Communications*, *5*, 4694. <http://doi.org/10.1038/ncomms5694>
- 642 Fries, P. (2001). Modulation of Oscillatory Neuronal Synchronization by Selective Visual  
643 Attention. *Science*, *291*(5508), 1560–1563. <http://doi.org/10.1126/science.1055465>
- 644 Fries, P., Roelfsema, P. R., Engel, A. K., König, P., & Singer, W. (1997). Synchronization of  
645 oscillatory responses in visual cortex correlates with perception in interocular rivalry.  
646 *Proceedings of the National Academy of Sciences of the United States of America*,  
647 *94*(23), 12699–12704.
- 648 Gilbert, C. D., & Sigman, M. (2007). Brain states: top-down influences in sensory processing.  
649 *Neuron*, *54*(5), 677–696. <http://doi.org/10.1016/j.neuron.2007.05.019>
- 650 Granger, C. (1969). Investigating causal relations by econometric models and cross-spectral  
651 methods. *Econometrica*, *37*(3), 424–438.
- 652 Gray, C. M., & Singer, W. (1989). Stimulus-specific neuronal oscillations in orientation  
653 columns of cat visual cortex. *Proceedings of the National Academy of Sciences of the*  
654 *United States of America*, *86*(5), 1698–1702.
- 655 Gray, C. M., König, P., Engel, A. K., & Singer, W. (1989). Oscillatory responses in cat visual  
656 cortex exhibit inter-columnar synchronization which reflects global stimulus properties.  
657 *Nature*, *338*(6213), 334–337. <http://doi.org/10.1038/338334a0>
- 658 Grothe, I., Neitzel, S. D., Mandon, S., & Kreiter, A. K. (2012). Switching neuronal inputs by  
659 differential modulations of gamma-band phase-coherence. *The Journal of Neuroscience*  
660 *: the Official Journal of the Society for Neuroscience*, *32*(46), 16172–16180.  
661 <http://doi.org/10.1523/JNEUROSCI.0890-12.2012>
- 662 Hilgetag, C. C., O'Neill, M. A., & Young, M. P. (1996). Indeterminate organization of the  
663 visual system. *Science*, *271*(5250), 776–777.
- 664 Hoogenboom, N., Schoffelen, J.-M., Oostenveld, R., Parkes, L. M., & Fries, P. (2006).

- 665 Localizing human visual gamma-band activity in frequency, time and space.  
666 *NeuroImage*, 29(3), 764–773. <http://doi.org/10.1016/j.neuroimage.2005.08.043>
- 667 Jia, X., Tanabe, S., & Kohn, A. (2013). Gamma and the Coordination of Spiking Activity in  
668 Early Visual Cortex. *Neuron*, 77(4), 762–774. <http://doi.org/10.1016/j.neuron.2012.12.036>
- 669 Kreiter, A. K., & Singer, W. (1996). Stimulus-dependent synchronization of neuronal  
670 responses in the visual cortex of the awake macaque monkey. *The Journal of*  
671 *Neuroscience : the Official Journal of the Society for Neuroscience*, 16(7), 2381–2396.
- 672 Lee, J. H., Whittington, M. A., & Kopell, N. J. (2013). Top-down beta rhythms support  
673 selective attention via interlaminar interaction: a model. *PLoS Computational Biology*,  
674 9(8), e1003164. <http://doi.org/10.1371/journal.pcbi.1003164>
- 675 Lewis, C. M., Bosman, C. A., Womelsdorf, T., & Fries, P. (2016). Stimulus-induced visual  
676 cortical networks are recapitulated by spontaneous local and interareal synchronization.  
677 *Proceedings of the National Academy of Sciences of the United States of America*,  
678 113(5), E606–15. <http://doi.org/10.1073/pnas.1513773113>
- 679 Maris, E., & Oostenveld, R. (2007). Nonparametric statistical testing of EEG- and MEG-data.  
680 *Journal of Neuroscience Methods*, 164(1), 177–190.  
681 <http://doi.org/10.1016/j.jneumeth.2007.03.024>
- 682 Markov, N. T., Vezoli, J., Chameau, P., Falchier, A., Quilodran, R., Huissoud, C., et al.  
683 (2014). Anatomy of hierarchy: feedforward and feedback pathways in macaque visual  
684 cortex. *J Comp Neurol*, 522(1), 225–259. <http://doi.org/10.1002/cne.23458>
- 685 Michalareas, G., Vezoli, J., van Pelt, S., Schoffelen, J.-M., Kennedy, H., & Fries, P. (2016).  
686 Alpha-Beta and Gamma Rhythms Subserve Feedback and Feedforward Influences  
687 among Human Visual Cortical Areas. *Neuron*, 89(2), 384–397.  
688 <http://doi.org/10.1016/j.neuron.2015.12.018>
- 689 Oostenveld, R., Fries, P., Maris, E., & Schoffelen, J.-M. (2011). FieldTrip: Open source  
690 software for advanced analysis of MEG, EEG, and invasive electrophysiological data.  
691 *Computational Intelligence and Neuroscience*, 2011, 156869.  
692 <http://doi.org/10.1155/2011/156869>
- 693 Paxinos, G., Huang, X., & Toga, A. W. (1999). The Rhesus Monkey Brain in Stereotaxic  
694 Coordinates. San Diego: Academic Press.
- 695 Percival, D. B., & Walden, A. T. (1993). Spectral Analysis for Physical Applications.  
696 Cambridge University Press.
- 697 Pinotsis, D. A., Brunet, N., Bastos, A., Bosman, C. A., Litvak, V., Fries, P., & Friston, K. J.  
698 (2014). Contrast gain control and horizontal interactions in V1: A DCM study.  
699 *NeuroImage*, 92, 143–155. <http://doi.org/10.1016/j.neuroimage.2014.01.047>
- 700 Richter, C. G., Thompson, W. H., Bosman, C. A., & Fries, P. (2015). A jackknife approach to  
701 quantifying single-trial correlation between covariance-based metrics undefined on a  
702 single-trial basis. *NeuroImage*, 114, 57–70.  
703 <http://doi.org/10.1016/j.neuroimage.2015.04.040>
- 704 Rohlfing, T., Kroenke, C. D., Sullivan, E. V., Dubach, M. F., Bowden, D. M., Grant, K. A., &  
705 Pfefferbaum, A. (2012). The INIA19 Template and NeuroMaps Atlas for Primate Brain  
706 Image Parcellation and Spatial Normalization. *Frontiers in Neuroinformatics*, 6, 27.  
707 <http://doi.org/10.3389/fninf.2012.00027>
- 708 Rubehn, B., Bosman, C., Oostenveld, R., Fries, P., & Stieglitz, T. (2009). A MEMS-based  
709 flexible multichannel ECoG-electrode array. *Journal of Neural Engineering*, 6(3), 036003.  
710 <http://doi.org/10.1088/1741-2560/6/3/036003>
- 711 Salazar, R. F., Dotson, N. M., Bressler, S. L., & Gray, C. M. (2012). Content-specific fronto-  
712 parietal synchronization during visual working memory. *Science*, 338(6110), 1097–1100.  
713 <http://doi.org/10.1126/science.1224000>
- 714 Stein, von, A., vonStein, A., Chiang, C., König, P., & König, P. (2000). Top-down processing  
715 mediated by interareal synchronization. *Proceedings of the National Academy of*  
716 *Sciences of the United States of America*, 97(26), 14748–14753.  
717 <http://doi.org/10.1073/pnas.97.26.14748>
- 718 Stetson, C., & Andersen, R. A. (2014). The parietal reach region selectively anti-

- 719 synchronizes with dorsal premotor cortex during planning. *The Journal of Neuroscience* :  
720 *the Official Journal of the Society for Neuroscience*, 34(36), 11948–11958.  
721 <http://doi.org/10.1523/JNEUROSCI.0097-14.2014>
- 722 Tallon-Baudry, C., Bertrand, O., Delpuech, C., & Pernier, J. (1996). Stimulus specificity of  
723 phase-locked and non-phase-locked 40 Hz visual responses in human. *The Journal of*  
724 *Neuroscience : the Official Journal of the Society for Neuroscience*, 16(13), 4240–4249.
- 725 Taylor, K., Mandon, S., Freiwald, W. A., & Kreiter, A. K. (2005). Coherent oscillatory activity  
726 in monkey area v4 predicts successful allocation of attention. *Cereb Cortex*, 15(9), 1424–  
727 1437. <http://doi.org/10.1093/cercor/bhi023>
- 728 Thomson, D. J. (1977). Spectrum Estimation Techniques for Characterization and  
729 Development of WT4 Waveguide-I. *Bell System Technical Journal*, 56(9), 1769–1815.  
730 <http://doi.org/10.1002/j.1538-7305.1977.tb00591.x>
- 731 Thomson, D. J. (1982). Spectrum estimation and harmonic analysis. *Proceedings of the*  
732 *IEEE*, 70(9), 1055–1096. <http://doi.org/10.1109/proc.1982.12433>
- 733 Trongnetrpunya, A., Nandi, B., Kang, D., Kocsis, B., Schroeder, C. E., & Ding, M. (2015).  
734 Assessing Granger Causality in Electrophysiological Data: Removing the Adverse  
735 Effects of Common Signals via Bipolar Derivations. *Frontiers in Systems Neuroscience*,  
736 9(32), 189. <http://doi.org/10.3389/fnsys.2015.00189>
- 737 Van Essen, D. C. (2012). Cortical cartography and Caret software. *NeuroImage*, 62(2), 757–  
738 764. <http://doi.org/10.1016/j.neuroimage.2011.10.077>
- 739 van Kerkoerle, T., Self, M. W., Dagnino, B., Gariel-Mathis, M.-A., Poort, J., van der Togt, C.,  
740 & Roelfsema, P. R. (2014). Alpha and gamma oscillations characterize feedback and  
741 feedforward processing in monkey visual cortex. *Proceedings of the National Academy*  
742 *of Sciences of the United States of America*, 111(40), 14332–14341.  
743 <http://doi.org/10.1073/pnas.1402773111>
- 744 Vinck, M., van Wingerden, M., Womelsdorf, T., Fries, P., & Pennartz, C. M. A. (2010). The  
745 pairwise phase consistency: a bias-free measure of rhythmic neuronal synchronization.  
746 *NeuroImage*, 51(1), 112–122. <http://doi.org/10.1016/j.neuroimage.2010.01.073>
- 747 Vinck, M., Womelsdorf, T., Buffalo, E. A., Desimone, R., & Fries, P. (2013). Attentional  
748 modulation of cell-class-specific gamma-band synchronization in awake monkey area v4.  
749 *Neuron*, 80(4), 1077–1089. <http://doi.org/10.1016/j.neuron.2013.08.019>
- 750 Welch, P. (1967). The use of fast Fourier transform for the estimation of power spectra: A  
751 method based on time averaging over short, modified periodograms. *IEEE Transactions*  
752 *on Audio and Electroacoustics*, 15(2), 70–73. <http://doi.org/10.1109/TAU.1967.1161901>
- 753 Womelsdorf, T., Fries, P., Mitra, P. P., & Desimone, R. (2006). Gamma-band synchronization  
754 in visual cortex predicts speed of change detection. *Nature*, 439(7077), 733–736.  
755 <http://doi.org/10.1038/nature04258>
- 756 Wyart, V., & Tallon-Baudry, C. (2008). Neural dissociation between visual awareness and  
757 spatial attention. *The Journal of Neuroscience : the Official Journal of the Society for*  
758 *Neuroscience*, 28(10), 2667–2679. <http://doi.org/10.1523/JNEUROSCI.4748-07.2008>  
759